

UCLA

UCLA Previously Published Works

Title

Influence of phosphate concentration on amine, amide, and hydroxyl CEST contrast

Permalink

<https://escholarship.org/uc/item/8wx8q6kg>

Journal

Magnetic Resonance in Medicine, 85(2)

ISSN

0740-3194

Authors

Yao, Jingwen
Wang, Chencai
Ellingson, Benjamin M

Publication Date

2021-02-01

DOI

10.1002/mrm.28481

Peer reviewed



Published in final edited form as:

Magn Reson Med. 2021 February ; 85(2): 1062–1078. doi:10.1002/mrm.28481.

Influence of phosphate concentration on amine, amide, and hydroxyl chemical exchange saturation transfer (CEST) contrast

Jingwen Yao, MS^{1,2,3}, Chencai Wang, PhD^{1,2}, Benjamin M. Ellingson, PhD^{1,2,3,4,*}

¹UCLA Brain Tumor Imaging Laboratory (BTIL), Center for Computer Vision and Imaging Biomarkers, University of California, Los Angeles, Los Angeles, CA

²Department of Radiological Sciences, David Geffen School of Medicine, University of California, Los Angeles, Los Angeles, CA

³Department of Bioengineering, Henry Samueli School of Engineering and Applied Science, University of California Los Angeles, Los Angeles, CA

⁴Department of Psychiatry and Biobehavioral Sciences, David Geffen School of Medicine, University of California, Los Angeles, Los Angeles, CA

Abstract

Purpose: To evaluate the influence of phosphate on amine, amide, and hydroxyl CEST contrast using Bloch-McConnell simulations applied to physical phantom data.

Methods: Phantom solutions of four representative metabolites with exchangeable protons – glycine ($-\alpha\text{NH}_2$), creatine ($-\eta\text{NH}_2$), egg white protein ($-\text{NH}$), and glucose ($-\text{OH}$) – were prepared at different pH levels (5.6–8.9) and phosphate concentrations (5–80 mM). CEST images of the phantom were collected with CEST-EPI sequence at 3T. The CEST data were then fitted to full Bloch-McConnell equation simulations to estimate the exchange rate constants. With the fitted parameters, simulations were performed to evaluate the intracellular and extracellular contributions of CEST signals in normal brain tissue and brain tumors, as well as in dynamic glucose enhanced (DGE) experiments.

Results: The exchange rates of α -amine and hydroxyl protons were found to be highly dependent on both pH and phosphate concentrations, while the exchange rates of η -amine and amide protons were pH-dependent, albeit not catalyzed by phosphate. With phosphate being predominantly intracellular, CEST contrast of α -amine exhibited a higher sensitivity to changes in the extracellular microenvironment. Simulations of DGE signals demonstrated that the contrast between normal and tumor tissue was mostly due to the extracellular CEST effect.

*Corresponding author: Benjamin M. Ellingson, Ph.D., Director, UCLA Brain Tumor Imaging Laboratory (BTIL), Professor of Radiology and Psychiatry, Departments of Radiological Sciences and Psychiatry, David Geffen School of Medicine, University of California, Los Angeles, 924 Westwood Blvd., Suite 615, Los Angeles, CA 90024 (bellingson@mednet.ucla.edu). Phone: 310-481-7572, Fax: 310-794-2796.

Data Availability Statement

The MATLAB code used for CEST signal Bloch-McConnell equation simulation and the simulation for creating the plots in Fig. 1 and Fig. 6 in this study is publicly available on GitHub (https://github.com/Jingwen-Yao/CESTsim_5pool_wMTC). Imaging data will be provided upon request.

Conclusion: The proton exchange rates in some metabolites can be greatly catalyzed by the presence of phosphate at physiological concentrations, which substantially alters the CEST contrast. Catalytic agents should be considered as confounding factors in future CEST-MRI research. This new dimension may also benefit the development of novel phosphate-sensitive imaging methods.

Keywords

chemical exchange saturation transfer (CEST); phosphate; chemical exchange; proton exchange

Introduction

Phosphate is an essential building block for cell membranes, DNA, and proteins. Residing mostly within the cells, it can take the form of adenosine triphosphate (ATP), phosphocreatine, phosphate esters, or inorganic phosphate, serving as an important component of energy metabolism, intracellular pH buffering, and kinase signaling.¹ In diseases such as cancer, increased extracellular and intracellular phosphate concentrations have been reported to promote cell proliferation.²⁻⁴

Despite being the predominant intracellular proton exchange catalyst, the effect of phosphate on CEST remains largely understudied. CEST exploits the chemical exchange of labile protons on exogenous or endogenous molecules with water to create MR contrast.⁵ By tuning the CEST sequence parameters to target exchangeable protons with different exchange rates and offset frequencies, CEST contrasts with specific metabolite-weightings can be achieved. The most researched CEST contrast is the amide proton transfer (APT) imaging, which targets the amide proton on mobile peptides and proteins.⁶⁻⁹ Other metabolite-weighted CEST imaging methods include brain glutamate imaging,¹⁰ muscle creatine imaging,¹¹ glycosaminoglycan imaging of cartilage,¹² and glucose imaging.¹³ CEST contrast can also be influenced by many factors that affect the chemical exchange rate, including pH, which has been explored to characterize brain tumor acidity,^{14,15} early cerebral ischemic changes,⁶ and pH mapping of the kidneys.¹⁶

Phosphate has been reported to increase the exchange rate of amine ($-NH_2$) and hydroxyl ($-OH$) protons by 10 kHz under physiological conditions.¹⁷ In the current study, we aim to characterize the effect of phosphate concentration on a variety of CEST contrasts, by performing phantom experiments and physical simulations using four representative metabolites with exchangeable protons: glycine ($-\alpha NH_2$), creatine ($-\eta NH_2$), egg white protein ($-NH$), and glucose ($-OH$). We hypothesized that phosphate would have differing effects on different CEST contrasts, and that catalytic agents should be considered as confounding factors in future CEST-MRI researches, to more accurately understand the underlying systems.

Methods

Phantom Preparation

We prepared glycine (Sigma-Aldrich), creatine (Sigma-Aldrich), egg white protein (commercial), and D-glucose (Sigma-Aldrich) phantom solutions at different phosphate concentrations (ranging from 5 to 80 mM) and pH levels (ranging from 5.6 to 8.9). Detailed information on phantom compositions can be found in Table 1. All sample solutions were pipetted from highly concentrated stock solutions to ensure the precision of concentrations. We used monobasic and dibasic potassium phosphate (KH₂PO₄ and K₂HPO₄, Sigma-Aldrich) as buffer agent and catalyst of the proton exchange process. KH₂PO₄ and K₂HPO₄ concentrations were calculated from phosphate pK_a (6.82), desired pH, and total phosphate concentration for each sample. pH was measured at room temperature with Accumet pH meter (Fisher Scientific, Massachusetts, MN, USA), after mixing and pH adjusting using acid (HCl) and base (NaOH).

Proton Exchange Model

In general, the rate constant of proton exchange k_{ex} between water and exchangeable proton pools can be described by:

$$k_{ex} = k_0 + k_a[H^+] + k_b[OH^-] + \sum_i k_{ci}[catalyst]^{di} \quad \# [1]$$

Where k_0 , k_a , k_b , and k_{ci} represent the spontaneous, acid-catalyzed, base-catalyzed exchange rate constants, as well as the exchange rates contributed by other catalysts.

Assumption 1: The acid-catalyzed proton exchange can be ignored for exchange between water and amine (–NH₂) or amide (–NH) groups. The rate constant of proton transfer can often be calculated from¹⁸:

$$k_{transfer} = k_D \frac{10^{\Delta pK}}{1 + 10^{\Delta pK}} \quad \# [2]$$

Where $pK = pK(\text{acceptor}) - pK(\text{donor})$, and k_D is the rate constant for diffusion controlled encounter of the proton donor and acceptor, typically $10^{10} - 10^{11} \text{M}^{-1} \text{sec}^{-1}$.¹⁹ In the case of acid- or base-catalyzed proton exchange, H^+ or OH^- serves as proton donor/acceptor with $pK = 14$, and amino acid groups as proton acceptor/donor with pK ranging from 9 to 11.²⁰ Due to the large negative value of pK in the acid-catalyzed process, it is safe to assume that acid-catalyzed proton exchange has negligible contribution to the total exchange rate, under physiologically relevant pH. The glucose hydroxyl group, on the other hand, has a pK of 12.28,²¹ which would lead to a non-negligible contribution from the acid-catalyzed proton exchange when pH is lower than ~6. The amide proton exchange process is usually complicated by the neighboring carbonyl group and the local environment in peptides and proteins. Eriksson et al. have shown that the pH_{min} – the pH where acid- and base-catalyzed exchange rates become equal – is typically in the range of 2 to 4 for amide protons.^{22,23} Based on this, we also ignored acid-catalyzed proton exchanges in amide groups.

Assumption 2: The catalytic effect of inorganic phosphate species can be expressed as the sum of HPO_4^{2-} and $H_2PO_4^-$ catalyzed exchange. At room temperature, potassium phosphate has pK_a of 2.15, 6.82, and 12.38. As a result, the predominant forms of phosphate were HPO_4^{2-} and $H_2PO_4^-$ in the pH range of 5 to 9.

Given the above assumptions, we formulated the proton exchange rate model as:

$$k_{ex} = k_0 (+ k_a[H^+]) + k_b[OH^-] + k_{cA}[HPO_4^{2-}] + k_{cB}[H_2PO_4^-] \quad \#[3]$$

where k_{cA} and k_{cB} represent the HPO_4^{2-} and $H_2PO_4^-$ catalyzed exchange constants, respectively. The acid-catalyzed exchange rate term is only included for –OH group analysis.

CEST-MRI Acquisition

CEST images were collected using a multi-echo multi-slice CEST-EPI sequence¹⁵ on a Siemens 3T scanner (Prisma), with an off-resonance saturation train of three 100ms Gaussian pulses using a peak amplitude of 4.2 μ T for amine phantoms and 1.4 μ T for protein and glucose phantoms. The duty cycle of the RF irradiation was 70%. The non-selective saturation pulses were repeated before the EPI acquisition of each slice, to ensure sufficient spin labeling. Supplementary Fig. 1 demonstrated the schematic diagram of the sequence. Four acquisitions of reference images, with no RF irradiation, were performed at the beginning of the scan, followed by the acquisition of saturated images with off-resonance saturation frequency from –5.0 ppm to +5.0 ppm. The other acquisition parameters were as follows: TR = 10 s, TEs = 14.0 ms and 34.1 ms, FOV = 217 \times 240 mm, matrix size = 116 \times 128, slice thickness = 4.0 mm with no inter-slice gap, slice number = 24, partial Fourier = 6/8, GRAPPA = 3, and bandwidth = 1628 Hz/pixel. All experiments were performed at room temperature.

CEST Post-Processing

Post-processing of CEST data consisted of motion correction, z -spectral based B_0 correction,²⁴ followed by quantification of magnetization transfer ratio asymmetry (MTR_{asym}) using equation: $MTR_{asym}(\omega) = (S(-\omega) - S(\omega)) / S_0$, where $S(\omega)$ was the amount of bulk water signal available after the saturation pulse with offset frequency ω and S_0 was the signal available without application of RF saturation. MTR_{asym} was calculated for each voxel and averaged across the width of 0.4 ppm around 3.0 ppm for glycine, 1.9 ppm for creatine, 3.5 ppm for egg white protein, and 1.3 ppm for glucose. The MTR_{asym} from the first (TE = 14.0 ms) and second (TE = 34.1 ms) gradient echoes were averaged to increase the available SNR. We manually created the regions of interest (ROIs) for each sample (about 20 mm³ each) and calculated the mean and standard deviation of MTR_{asym} . The mean of MTR_{asym} was used in subsequent fitting of the Bloch-McConnell equation simulation. All the post-processing of data was performed on MATLAB (Release 2019b, MathWorks, Natick, MA).

Parameter Fitting with Multi-Pool Bloch-McConnell Equation Simulation

We have adopted the multi-pool CEST model described by Zaiss et al. for simulating the CEST effect using Bloch-McConnell equations (BME),²⁵ with adaptation to accommodate more than two exchange pools, as well as to include semi-solid macromolecule magnetic transfer (MT) effect. The sequence parameters used in the phantom experiments were applied in the BME simulation. Each 100 ms Gaussian pulse was approximated with a train of 101 hard pulses. The evolution of magnetization was simulated and the transverse magnetization of the 10th acquisition (equivalent to 3×10 Gaussian saturation pulses) was used for fitting, to ensure a steady state signal. The results were then applied to the mean MTR_{asym} measurements from all phantom samples, to solve for the best fitting exchange rate constants k_0 , k_a , k_b , k_{cA} , and k_{cB} , the concentration of the exchanging proton species, and the water transverse relaxation time T_{2w} . All fittings and subsequent simulations were performed using MATLAB (Release 2019b, MathWorks, Natick, MA).

For the egg white protein phantom simulation, three exchange pools (water, amine, and amide proton) and the semi-solid MT effect were included in the simulation fitting. We assumed that the amine proton exchange characteristics were the same as in glycine phantom, and that the exchange rate of semi-solid MT pool was 20 s^{-1} with no pH or phosphate concentration dependency.

The proton exchange rate parameters that yielded the best-fit to the experimental data using least squares regression were retained and used for subsequent analyses. The least square regression was performed with MATLAB using functions *lsqcurvefit* and *nlinfit* in two stages. First, we used the negative offset z -spectrum data of the sample with the lowest MTR_{asym} to find the water T_2 , and semi-solid MT pool fraction in the case of egg white phantom. At the second stage, we applied the obtained T_2 and MT pool fraction to the simulation and performed the fitting for exchangeable proton concentrations and exchange rate constants. In both stages, the *lsqcurvefit* function with trust-region-reflective algorithm was used to obtain rough estimates, which were then used as initial guesses for the *nlinfit* function with the Levenburg–Marquardt algorithm, to obtain the final parameter estimates. Since the concentration, exchange rate, and T_2 parameters are positive by nature, the absolute values of the parameters were used in *nlinfit* to avoid setting the lower bound. The residual and the Jacobian of *nlinfit* were used to evaluate the confidence interval of the fitted parameters with function *nlparci*.

CEST Simulation of Normal Brain Tissue and Brain Tumor

To understand how the different intracellular and extracellular phosphate concentration might affect the amine and amide CEST contrast, four tissue compartments were simulated, including the intra- and extracellular compartments for both normal brain tissue and brain tumors. Water T_1 and T_2 values were adopted from literature values for normal white matter and glioma (normal tissue: $T_1 = 0.832 \text{ s}$, $T_2 = 0.110 \text{ s}$; tumor tissue: $T_1 = 1.558 \text{ s}$, $T_2 = 0.160 \text{ s}$).^{26–28} Phosphate concentrations were assumed to be the same in normal and tumor tissue, with intracellular concentration of 20 mM and extracellular concentration of 1 mM. Increases in cytosolic protein,⁷ amino acid,²⁹ and glucose concentration³⁰ have been reported in tumors, while creatine concentration was reported to decrease²⁹ in brain tumors.

The other assumptions of the tissue parameters used in the simulation included: higher amine and amide concentration in the intracellular compartment; equally distributed glucose concentration³¹; increases in extracellular amine concentration, contributed from increased amino acid demand and uptake,³² increased glutamate release,^{33,34} and increased extracellular protein and peptides.³⁵ The detailed tissue parameters and sequence parameters used in the simulation can be found in Table 2. The combined CEST contrast was calculated by assuming that 3/4 of the water proton signal arose from intracellular space and 1/4 from extracellular space for normal tissue, while for brain tumor tissue the signal was assumed arise half-and-half from intra- and extracellular space.³⁵

CEST Simulation of Dynamic Glucose Enhanced (DGE) MRI

We also simulated the time evolution of the DGE signal, in order to have a qualitative understanding of the intra- and extracellular contribution of the signal change. We modified the compartmental model for fluorodeoxyglucose (FDG) PET³⁶ to include three compartments: plasma, extracellular space, and intracellular space (Fig. 1a). The concentration of externally introduced glucose in each compartment was denoted as C_p , C_e , and C_i , respectively. The exchange rates between the compartments were adopted and modified from a previous FDG study,³⁷ with detailed parameter values listed in Table 2. The exchange rates between plasma and brain tissue (k_1 , k_2) and the metabolic rate of glucose conversion to glucose-6-phosphate (k_3) were adopted directly from the PET study. In addition, we assumed that tumor tissue exhibited faster exchange rates than normal white matter and had exchange rates similar to grey matter. The exchange rates from extracellular to intracellular compartment were assumed to be similar to that from plasma to brain tissue, with much smaller efflux rates. The simulated dynamic glucose concentrations at each time point were added to the endogenous concentrations for CEST contrast simulation. The CEST sequence parameters used for simulation are listed in Table 2 and the time evolution of DGE signal was calculated as the normalized signal change at 1.2 ppm using the equation: $S/S_0 = (S_{baseline}(1.2ppm) - S(1.2ppm))/S_0$, where $S(\omega)$ is the water signal after the saturation pulse with offset frequency ω at baseline and at each timepoint.

Results

We performed phantom experiments with four representative metabolites with exchangeable protons with different phosphate concentrations at different pH levels (Table 1). The measurements of phantom MTR_{asym} were then fitted with full Bloch-McConnell equation simulations of the CEST sequence. The results of BME fitting and the confidence intervals (CI) of the fitted parameters were summarized in Table 3. We subsequently used the best-fit parameters to simulate the *in vivo* CEST signal, to better understand the source of contrasts.

Phantom Experiments and Bloch-McConnell Equation Fitting

The phantom experiment results for glycine was shown in Fig. 2a–d. Both pH and phosphate concentration affected the CEST characteristics of glycine. Under the same phosphate concentration, glycine exhibited higher MTR_{asym} at lower pH. At a phosphate concentration of 80 mM (Fig. 2d), the high MTR_{asym} at acidic pH was largely reduced, compared to at 5 mM phosphate concentration (Fig. 2b). MTR_{asym} at 3.0 ppm from all phantom samples were

fitted with Bloch-McConnell simulations and plotted in Fig. 2e–f. The Bloch-McConnell simulation fitted well with the physical phantom measurements ($R^2 = 1.00$, Fig. 2e–f). The fitted exchangeable proton concentration was 181.73 mM (CI: 176.46 – 187.00 mM). The result was slightly lower than but still largely in agreement with the hypothesis that each glycine molecule contributed two exchangeable amine protons. Results also confirmed the high dependency of amine CEST contrast on phosphate concentration ($k_{cA} = 2.26 \times 10^5 \text{ s}^{-1} \text{ M}^{-1}$, $k_{cB} = 7.55 \times 10^3 \text{ s}^{-1} \text{ M}^{-1}$) and on pH ($k_b = 3.45 \times 10^{10} \text{ s}^{-1} \text{ M}^{-1}$). Using the fitted parameters, we calculated the proton exchange rate with the equation:

$k_{ex} = k_0 + k_b[\text{OH}^-] + k_{cA}[\text{HPO}_4^{2-}] + k_{cB}[\text{H}_2\text{PO}_4^-]$, as plotted in Fig. 2g. At lower pH, the exchange rates at different phosphate concentrations could differ by one order of magnitude. Lastly, the image of glycine phantom MTR_{asym} map was demonstrated in Fig. 2h.

Fig. 3a–d plotted the phantom experiment results for creatine. Creatine CEST characteristics changed drastically with different pH levels. However, they were not affected by different phosphate concentrations. The peak of MTR_{asym} contrast at around 1.9 ppm increased with increasing pH, peaking at pH 7.6, and decreasing at higher pH levels with a broadened line width, indicating the entering to fast exchange regime (Fig. 3b,d). The BME fitting of MTR_{asym} at 1.9 ppm from all phantom samples was shown in Fig. 3e–f ($R^2 = 0.99$). The amine proton concentration was fitted to be 134.33 mM (CI: 130.58 – 138.17.20 mM). The fitting results also agreed with the observation of high pH dependency ($k_b = 1.34 \times 10^9 \text{ s}^{-1} \text{ M}^{-1}$) but low phosphate concentration dependency ($k_{cA} = 630.43 \text{ s}^{-1} \text{ M}^{-1}$, $k_{cB} = 0 \text{ s}^{-1} \text{ M}^{-1}$). With these fitting parameters, we calculated the proton exchange rate, as plotted in Fig. 3g. The image of creatine phantom MTR_{asym} map was shown in Fig. 3h.

Fig. 4a–d depicted the phantom experiment results for egg white protein. The MTR_{asym} with offset frequency 3.00 ppm or higher demonstrated similar features at low and high phosphate concentration (Fig. 4b,d). However, changes in MTR_{asym} were observed in the range of 1.0ppm to 3.0ppm, which was similar to the trend observed in glycine phantom. At a phosphate concentration of 5 mM, MTR_{asym} increased with decreasing pH (Fig. 4b). The elevated MTR_{asym} at acidic pH was then largely suppressed when phosphate concentration reached 80 mM (Fig. 4d). The BME fitting results were plotted in Fig. 4e–f. The amide and amine concentrations were fitted to be 46.46 mM and 46.44 mM, respectively. The semi-solid macromolecule pool fraction was fitted to be 3.45×10^{-6} . APT contrast had a high pH dependency ($k_b = 7.53 \times 10^7 \text{ s}^{-1} \text{ M}^{-1}$) but low phosphate concentration dependency ($k_{cA} = 8.52 \text{ s}^{-1} \text{ M}^{-1}$, $k_{cB} = 13.92 \text{ s}^{-1} \text{ M}^{-1}$). This was also demonstrated by the proton exchange plot in Fig. 4g. An egg white protein phantom MTR_{asym} image map was shown in Fig. 4h.

Lastly, we used a D-glucose phantom to understand its CEST characteristics and dependencies on pH and phosphate concentrations (Fig. 5a–d). Glucose predominantly took the form of pyranose ring in the solution. The ratio of the α and β pyranose configuration has been reported to be 0.36/0.64. The C-1 –OH group has a chemical shift at 2.08 ppm for α form and 2.88 ppm for β form. The –OH groups at C-2, 3, and 4 have similar chemical shift at 1.28 ppm. And the C-6 –OH group has a chemical shift at 0.66 ppm.^{38,39} We were able to observe two main peaks on the MTR_{asym} plot (Fig. 5b), one close to 1.28 ppm, the other around 2.88 ppm. The 0.66 ppm peak could be too close to the water resonance

frequency to be observed at 3T. The 2.08 ppm peak generally had a smaller pool fraction and might be coalesced with the other peaks due to its position. The MTR_{asym} peaks observed at 5 mM phosphate concentration were suppressed when using 80 mM phosphate as buffer. The BME fitting results of the 1.28 ppm proton pool were demonstrated in Fig. 5e–f. The hydroxyl proton concentration was fitted to be 267.32 mM (CI: 204.05 – 330.59 mM), consistent with the hypothesis that glucose molecule contributed three hydroxyl protons that resonated at 1.28 ppm. Glucose CEST contrast has a high dependency on both pH ($k_a = 2.64 \times 10^8 \text{ s}^{-1}\text{M}^{-1}$, $k_b = 3.93 \times 10^9 \text{ s}^{-1}\text{M}^{-1}$) and phosphate concentration ($k_{cA} = 6.46 \times 10^4 \text{ s}^{-1}\text{M}^{-1}$, $k_{cB} = 2.35 \times 10^4 \text{ s}^{-1}\text{M}^{-1}$). Fig. 5g shows how the phosphate-catalyzed effect and the acid- and base-catalyzation both contributed to the total exchange rate. The image of the glucose phantom MTR_{asym} map was shown in Fig. 5h.

BME Simulation of Amine, Amide CEST contrast and DGE time curve

Using the best-fit exchange rate parameters obtained from the physical phantoms, the intra- and extracellular CEST effect within normal brain or tumor tissue were evaluated (Fig. 6). With two CEST saturation schemes at high and low saturation pulse strengths, we targeted fast-exchanging amine protons and slow-exchanging amide protons, respectively. Compared to the amine CEST simulation, the MTR_{asym} spectrum of amide CEST in the intracellular compartment showed sharper peaks at amide proton resonance frequency (3.5 ppm) and creatine proton resonance frequency (2.0 ppm), although the peak amplitudes were similar (Fig. 6b,e). The greater difference presented in the tumor extracellular compartment simulation, where significantly higher MTR_{asym} was observed at α -amine proton resonance frequency (3.0 ppm). When combining the intra- and extracellular compartments together, both amine and amide CEST effect had predominant contribution from intracellular compartment. However, the change in amine and amide CEST in tumor tissue compared to normal tissue had different sources, with extracellular area changes contributing more to the amine CEST tumor tissue contrast (63%) and intracellular area contributing more to amide CEST contrast (70%).

We also evaluated the dynamic CEST signal change during DGE imaging. The kinetics modeling of externally administered glucose concentration in different compartments demonstrated a fast initial increase in extracellular concentration, followed by a slower increase in intracellular concentration (Fig. 1b). The extracellular glucose concentration in tumor tissue was only slightly higher than that of normal brain tissue under the current simulation parameter settings, while the predominant total tissue concentration difference came from the intracellular space. With the full BME simulation of CEST effect, we found that the CEST signal difference between normal and tumor tissue was mostly contributed from the extracellular space (Fig. 1c).

Discussion

Glycine

Glycine is the simplest amino acid. It has a single hydrogen atom as its side chain. We used glycine to evaluate the exchange rate characteristics of $-\alpha\text{NH}_2$ group in amino acids. At low phosphate concentration, MTR_{asym} at 3.0ppm increased with decreasing pH and peaked

around pH 6.0 to 6.5. As the pH approached 7.4, the proton exchange rate went from intermediate exchange regime to fast exchange regime, leading to decreased CEST labeling efficiency. With increasing phosphate concentration, the curve of MTR_{asym} shifted toward lower pH (Fig. 2e). The catalytic effect of phosphate caused the saturation efficiency to drop even when limited base-catalysis was present. The BME fitting confirmed the high dependency of amine CEST contrast on phosphate concentration and on pH. Although the base-catalyzed exchange rate constant of glycine proton has not been reported before, k_b of glutamate with a similar $-\alpha\text{NH}_2$ group, was reported to have $k_b = 2.52 \times 10^{10} - 4.50 \times 10^{10} \text{ s}^{-1} \text{ M}^{-1}$,^{40,41} which agrees well with our fitting results ($k_b = 3.45 \times 10^{10} \text{ s}^{-1} \text{ M}^{-1}$). With an intracellular phosphate concentration of about 60mM and pH of 7 at body temperature 37°C, the phosphate-catalyzed exchange rate was calculated to be $8.34 \times 10^3 \text{ s}^{-1}$, which contributed almost half of the total exchange rate $1.71 \times 10^4 \text{ s}^{-1}$. The high intracellular phosphate concentration might lead to the suppression of intracellular amine CEST contrast, resulting in a higher sensitivity to changes in extracellular environment.

Creatine

Creatine is one of the major metabolites in the cell bioenergetic system. It is of wide interest to image creatine non-invasively in muscle,¹¹ heart,⁴² and in pathological conditions including infarct and brain tumors.^{43,44} Creatine also possesses amine proton-like amino acids, but within a guanidinium group ($\text{HNC}(\text{NH}_2)_2$). The resonance stabilization of charge on the two $-\eta\text{NH}_2$ makes the cation form of creatine guanidinium group $(\text{NH}_2)_2^+$ a highly stable structure under neutral pH. This unique structure exhibited different proton transfer characteristics from $-\alpha\text{NH}_2$ group, with high pH dependency but low phosphate concentration dependency. From the BME fitting, the amine proton concentration was fitted to be 134.33 mM, which was lower than the expected 200 mM. The deviation from the hypothesis of four exchangeable protons in each creatine molecule was likely due to the deprotonation at high pH ($pK_a = 12.7$) and the intra-molecular cyclisation to creatinine at lower pH,⁴⁵ both leading to a reduction of the total number of exchangeable protons. An average number of exchanging guanidinium protons per creatine molecule of less than four was also reported by a previous quantitative creatine CEST study.⁴⁶ With the fitted exchange rate constants, we calculated the proton exchange rate under intracellular environment (phosphate concentration = 60mM, pH = 7, temperature = 37°C). The phosphate-catalyzed exchange rate was calculated to be 22.78 s^{-1} , contributing only about 6% of the total exchange rate 374.59 s^{-1} . This dominant base-catalyzed and weak buffer-catalyzed proton exchange was also reported previously.⁴⁶ The published exchange rate of creatine guanidinium protons at pH = 7 and body temperature ranged from 810 s^{-1} to 1190 s^{-1} .^{41,46} Our predicted values of exchange rates were smaller than the values reported by other groups, though within the same order of magnitude. The deviation may be due to our assumption that the exchange rate constants were independent of temperature. Characterizing the temperature dependency of creatine proton exchange rate was beyond the scope of this study and has been previously described.⁴⁷

Egg white protein

Generic egg white protein is an easily available source of a rich variety of proteins (Table 1) commonly used as a physical phantom for APT imaging.^{48,49} However, the complexity

arising from multiple exchangeable proton pools in addition to semi-solid macromolecular MT and nuclear Overhauser enhancement (NOE) effects makes accurate modeling difficult. Compared to amine phantoms, the goodness of fitting for amide MTR_{asym} was less optimal ($R^2 = 0.90$). The relatively low R^2 was mostly likely due to that the complexity of protein proton exchange could not be fully captured by the proposed three-proton pools exchange model with macromolecule MT effect. Protein amine and amide protons experience different microenvironments and shielding depending on the local protein structure and nearby side chains. This would lead to the broadening of CEST peaks as well as a distribution of exchange rates across these slightly different proton exchange species. With intracellular environment, the phosphate-catalyzed exchange rate only made trivial contribution to the total exchange rate of 46.98 s^{-1} , which was consistent with literature values of 22 s^{-1} to 280 s^{-1} .⁵⁰⁻⁵²

Glucose

In recent years, there has been increasing interest in using glucose CEST to investigate glucose uptake and metabolism, both in a steady state and dynamically.^{13,53,54} In the phantom experiment results, we observed suppression of all MTR_{asym} peaks at 80 mM phosphate concentration. This indicated a strong phosphate-catalyzed proton exchange at all $-OH$ sites, and that the exchange rate entered into fast exchange regime at high phosphate concentration. Instead of fitting all four exchangeable proton pools, we fitted the MTR_{asym} at the main proton resonance frequency (1.28 ppm) to limit the number of fitting parameters while still being able to capture the main CEST characteristics. The influence of the other exchange pools, especially the C-6 hydroxyl proton pool at 0.66 ppm, might have led to the small deviation of the fitting results from the phantom data ($R^2 = 0.95$). Higher field strength or spectroscopic methods would be needed to separate the effect. We demonstrated that the phosphate-catalyzed effect was most obvious around pH of 6.5, accelerating the exchange rate by one order of magnitude, while the acid- and base-catalyzed exchange rate contributed more at lower or higher pH. In the intracellular environment, the phosphate-catalyzed exchange rate was calculated to be $2.89 \times 10^3 \text{ s}^{-1}$, contributing more than 70% of the total exchange rate of $3.91 \times 10^3 \text{ s}^{-1}$. Glucose proton exchange rate at pH 7 and with 10 mM phosphate buffer was reported to be $2.56 \times 10^3 \text{ s}^{-1}$.⁴¹ Our result with the same condition was calculated to be $1.50 \times 10^3 \text{ s}^{-1}$, which was lower than literature values while within the same order of magnitude. This might be because the signal we observed at 1.28 ppm was a mixture of multiple proton pools, including the 0.66 ppm hydroxyl group, which was reported to have an exchange rate of 950 s^{-1} .⁴¹

Implications on Amine, Amide CEST, and DGE Contrasts

The majority of phosphate in human body resides in the intracellular space. We demonstrated with our simulation that the catalytic effect of phosphate on proton exchange would contribute differently to the intra- and extracellular CEST effects within normal brain and tumor tissue. The intracellular α -amine CEST contrast would be suppressed due to the high proton exchange rate, which was contributed from both non-acidic intracellular pH and higher phosphate concentration. The extracellular α -amine CEST contrast in tumor tissue, on the contrary, would benefit from the higher amino acid concentration, slower exchange rate, and increased extracellular volume fraction. These effects together would result in a

predominant amine CEST contrast between tumor and normal tissue arising from the extracellular space and a higher sensitivity to changes in extracellular pH. On the other hand, phosphate has little effect on APT contrast, leading to the contrast primarily arising from changes in the intracellular compartment.

Hydroxyl proton exchange process was also greatly catalyzed by phosphate. Recently, multiple studies have explored the use of DGE imaging to evaluate the perfusion, uptake, and metabolism of glucose, in both brain tumor mice models and human subjects. In these pioneering works, DGE contrast was quantified as the change in normalized signal over time and the area under the time curve. Due to constraints including contrast to noise ratio and limited time resolution, no analysis of the kinetic characteristics has yet been performed. With advances in techniques and the standardization of contrast injection and image acquisition schemes, the kinetics modeling of DGE signal would allow us to extract important information of the tumor metabolism. Here we modified the FDG PET compartmental model to include intra- and extracellular components and simulated the dynamic glucose CEST effect.³⁶ We found that despite the greater glucose concentration change in the intracellular compartment, the CEST signal contrast between normal and tumor tissue was mostly contributed from the extracellular compartment, due to the slower hydroxyl proton exchange rate from low pH and low phosphate concentration. We believe that taking the phosphate concentration gradient into consideration would be essential to accurately model the DGE kinetics in the future.

Limitations and Future Work

At field strength of 3T, CEST contrast often suffers from low specificity due to overlapping effects from direct water excitation and multiple exchange pools. One limitation of our phantom study is that for physical phantoms with multiple exchange pools (egg white protein and glucose phantom), the quantification of exchange rate constants using BME fitting may be less accurate. Although the current study provided experimental evidence of the effect of phosphate-catalyzed proton exchange, CEST experiments at higher field strength or spectroscopic approaches need to be conducted to achieve accurate exchange rate constants quantification.

In this study, we added phosphate concentration as one more layer of complexity to the CEST contrast dependencies. However, we are still only considering a simplified model of *in vivo* conditions. We have demonstrated that inorganic phosphate was an effective catalyst of proton exchange, leading to altered CEST contrast. However, the majority of intracellular phosphate is in the form of different organic phosphates, including phosphocreatine, adenosine triphosphate (ATP), phosphoglycerate, phospholipid, and other phosphate esters. Question remains whether the organic phosphate shares similar catalytic characteristics to inorganic phosphate. With the known inorganic phosphate rate constants obtained from current experiments, the catalytic effect of organic phosphate can be approximated using the Brønsted catalysis law, as the organic phosphate species contains phosphate groups with pK_a values similar to those of inorganic phosphate (Table 4). In order to achieve a more accurate evaluation of the *in vivo* conditions, future investigation needs to be done using organic phosphate. Nonetheless, extra caution is required when conducting CEST experiments, since

the majority of organic compounds contain exchangeable protons that might directly change the CEST signal, obscuring the catalytic effect. In addition, although a large portion of intracellular phosphate is bounded to large molecules (Table 4), including phospholipids, phosphorylated proteins, and DNA, the slower diffusion rate or immobility of these large molecules may lead to less effective catalysis. Future study could adopt liposome to evaluate if phosphate bounded to large molecules would still have sufficient general base catalytic effect.

Furthermore, other proton exchange catalysts that are abundant under physiological conditions, including carbonate, amine groups, and acetate, could also have substantial effect on CEST contrast.¹⁷ In addition to H^+ and OH^- dissociated from water, acidic, and basic groups in proteins and peptides could also serve as efficient acid- and base-catalysts, especially when in the close proximity of the exchangeable proton. Besides, temperature dependency of exchange rate constants also needs to be considered in future experiments. Lastly, phosphate concentrations might change in different populations and under different physiological or pathological conditions. Infants generally have higher serum phosphate levels than adults,⁵⁷ while their total brain metabolite phosphate concentrations tend to be lower.⁵⁸ During anaerobic exercise, phosphate is rapidly converted between species involved in cell energetics (inorganic phosphate, phosphocreatine, ATP). Hypo- or hyperphosphatemia may occur due to various endocrine and metabolic disorders, including parathyroid disease and chronic kidney diseases.⁵⁹ Thus, more work needs to be done to systematically characterize and identify major sources of CEST contrast under different physiological and pathological conditions.

In the simulation study, we have directly applied the high and low saturation powers (peak B_1 of 4.2 μT and 1.4 μT) used in phantom experiments for the two simulation saturation schemes. In order to explore the influence of saturation power on CEST signals, we have also performed a simulation with a range of different saturation powers, with peak B_1 ranging from 0.7 μT to 4.2 μT , as plotted in Supplementary Fig. 2. In the future, a more comprehensive optimization of the saturation power could be performed to maximize the contrast of interest.

The simulation of the dynamics of DGE signal was performed with parameters adopted from FDG PET studies. The timescale and the amplitude of DGE signal would likely be very different in actual cases, depending on technical factors including the contrast dosage and injection velocity, as well as biological factors including the glucose uptake and metabolic rate in different tissues. We demonstrated here only a qualitative example to show that due to the catalytic effect of local microenvironment, DGE signal change cannot be translated directly to change in glucose concentration in tissue, unlike in dynamic gadolinium-enhanced MRI or PET imaging. Specific kinetics models would need to be designed and tested for DGE time curve in the future.

Conclusion

In this study, we investigated the catalytic effect of phosphate on proton exchange of glycine, creatine, egg white protein, and glucose. We found that glycine amine CEST

contrast and glucose hydroxyl CEST contrast were greatly influenced by phosphate concentration, which would lead to a higher sensitivity to extracellular environment. While APT and creatine CEST contrast were not as affected by phosphate, leading to mostly intracellular sensitivity. Results suggest phosphate should be taken into account in future CEST-MRI research, potentially leading to new opportunities including non-invasive imaging approaches specific to phosphate biochemistry.

Supplementary Material

Refer to Web version on PubMed Central for supplementary material.

Acknowledgements

The study was funded by American Cancer Society (ACS) Research Scholar Grant (RSG-15-003-01-CCE), UCLA SPORE in Brain Cancer (NIH/NCI 1P50CA211015-01A1), and NIH/NCI (1R21CA223757-01).

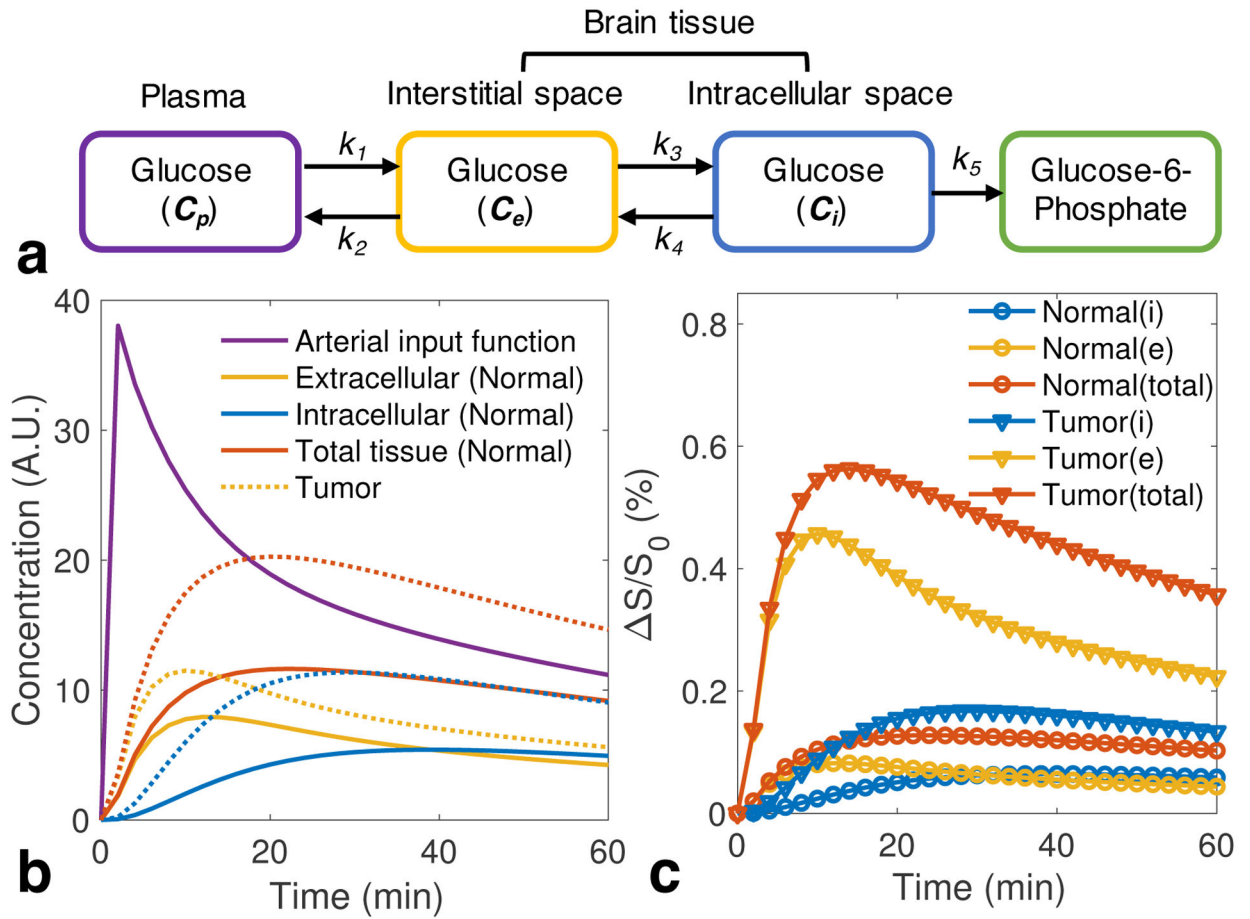
Reference

1. Takeda E, Taketani Y, Sawada N, Sato T, Yamamoto H. The regulation and function of phosphate in the human body. *Biofactors*. 2004;21(1–4):345–355. [PubMed: 15630224]
2. Bobko AA, Eubank TD, Driesschaert B, et al. Interstitial Inorganic Phosphate as a Tumor Microenvironment Marker for Tumor Progression. *Sci Rep-Uk*. 2017;7.
3. Ramirez CP, Fiedler D. Investigating the role of inorganic phosphate in tumor metabolism and metastasis. *Cancer & Metabolism*. 2014;2.
4. Qian YR, Wang X, Li YS, Cao YY, Chen XZ. Extracellular ATP a New Player in Cancer Metabolism: NSCLC Cells Internalize ATP In Vitro and In Vivo Using Multiple Endocytic Mechanisms. *Molecular Cancer Research*. 2016;14(11):1087–1096. [PubMed: 27578770]
5. Jones KM, Pollard AC, Pagel MD. Clinical applications of chemical exchange saturation transfer (CEST) MRI. *J Magn Reson Imaging*. 2018;47(1):11–27. [PubMed: 28792646]
6. Sun PZ, Cheung JS, Wang E, Lo EH. Association between pH-weighted endogenous amide proton chemical exchange saturation transfer MRI and tissue lactic acidosis during acute ischemic stroke. *J Cereb Blood Flow Metab*. 2011;31(8):1743–1750. [PubMed: 21386856]
7. Yan K, Fu ZM, Yang C, et al. Assessing Amide Proton Transfer (APT) MRI Contrast Origins in 9 L Gliosarcoma in the Rat Brain Using Proteomic Analysis. *Molecular Imaging and Biology*. 2015;17(4):479–487. [PubMed: 25622812]
8. Paech D, Windschuh J, Oberhollenzer J, et al. Assessing the predictability of IDH mutation and MGMT methylation status in glioma patients using relaxation-compensated multipool CEST MRI at 7.0 T. *Neuro Oncol*. 2018;20(12):1661–1671. [PubMed: 29733378]
9. Zhou JY, Payen JF, Wilson DA, Traystman RJ, van Zijl PCM. Using the amide proton signals of intracellular proteins and peptides to detect pH effects in MRI. *Nature Medicine*. 2003;9(8):1085–1090.
10. Cai KJ, Haris M, Singh A, et al. Magnetic resonance imaging of glutamate. *Nature Medicine*. 2012;18(2):302–306.
11. Kogan F, Haris M, Debrosse C, et al. In Vivo Chemical Exchange Saturation Transfer Imaging of Creatine (CrCEST) in Skeletal Muscle at 3T. *J Magn Reson Imaging*. 2014;40(3):596–602. [PubMed: 24925857]
12. Lee YH, Yang J, Jeong HK, Suh JS. Assessment of the patellofemoral cartilage: Correlation of knee pain score with magnetic resonance cartilage grading and magnetization transfer ratio asymmetry of glycosaminoglycan chemical exchange saturation transfer. *Magn Reson Imaging*. 2017;35:61–68. [PubMed: 27580516]
13. Walker-Samuel S, Ramasawmy R, Torrealdea F, et al. In vivo imaging of glucose uptake and metabolism in tumors. *Nature Medicine*. 2013;19(8):1067–+.

14. Harris RJ, Cloughesy TF, Liau LM, et al. Simulation, phantom validation, and clinical evaluation of fast pH-weighted molecular imaging using amine chemical exchange saturation transfer echo planar imaging (CEST-EPI) in glioma at 3 T. *NMR in Biomedicine*. 2016;29(11):1563–1576. [PubMed: 27717216]
15. Harris RJ, Yao J, Chakhoyan A, et al. Simultaneous pH-sensitive and oxygen-sensitive MRI of human gliomas at 3 T using multi-echo amine proton chemical exchange saturation transfer spin-and-gradient echo echo-planar imaging (CEST-SAGE-EPI). *Magn Reson Med*. 2018;80(5):1962–1978. [PubMed: 29626359]
16. Jones KM, Randtke EA, Yoshimaru ES, et al. Clinical Translation of Tumor Acidosis Measurements with AcidoCEST MRI. *Molecular Imaging and Biology*. 2017;19(4):617–625. [PubMed: 27896628]
17. Liepinsh E, Otting G. Proton exchange rates from amino acid side chains - Implications for image contrast. *Magnetic Resonance in Medicine*. 1996;35(1):30–42. [PubMed: 8771020]
18. Ehrenberg A, European Biophysical Societies Association., Marcus Wallenberg Foundation for International Cooperation in Science. Structure, dynamics, and function of biomolecules : the first EBSA workshop, a Marcus Wallenberg symposium. Berlin; New York: Springer-Verlag; 1987.
19. Eigen M. Kinetics of Proton Transfer Processes - General Introduction. *Discuss Faraday Soc*. 1965(39):7-&.
20. Turner GLE. *Crc Handbook of Chemistry and Physics - a Ready-Reference Book of Chemical and Physical Data, 70th Edition - Weast,Rc, Lide,Dr. Ann Sci*. 1991;48(5):496–497.
21. Nollet LML. Handbook of food analysis. In: *Food science and technology v 138*. 2nd ed. New York; Basel: Marcel Dekker.; 2004: FOODnetBASE. Restricted to UC campuses 10.1201/b11081.
22. Matthew JB, Richards FM. The Ph-Dependence of Hydrogen-Exchange in Proteins. *Journal of Biological Chemistry*. 1983;258(5):3039–3044.
23. Eriksson MAL, Hard T, Nilsson L. On the Ph-Dependence of Amide Proton-Exchange Rates in Proteins. *Biophys J*. 1995;69(2):329–339. [PubMed: 8527646]
24. Yao J, Ruan D, Raymond C, et al. Improving B0 Correction for pH-Weighted Amine Proton Chemical Exchange Saturation Transfer (CEST) Imaging by Use of k-Means Clustering and Lorentzian Estimation. *Tomography*. 2018;4(3):123–137. [PubMed: 30320212]
25. Zaiss M, Zu ZL, Xu JZ, et al. A combined analytical solution for chemical exchange saturation transfer and semi-solid magnetization transfer. *Nmr in Biomedicine*. 2015;28(2):217–230. [PubMed: 25504828]
26. Wansapura JP, Holland SK, Dunn RS, Ball WS Jr. NMR relaxation times in the human brain at 3.0 tesla. *J Magn Reson Imaging*. 1999;9(4):531–538. [PubMed: 10232510]
27. Oh J, Cha SM, Aiken AH, et al. Quantitative apparent diffusion coefficients and T2 relaxation times in characterizing contrast enhancing brain tumors and regions of peritumoral edema. *J Magn Reson Imaging*. 2005;21(6):701–708. [PubMed: 15906339]
28. Badve C, Yu A, Dastmalchian S, et al. MR Fingerprinting of Adult Brain Tumors: Initial Experience. *Am J Neuroradiol*. 2017;38(3):492–499. [PubMed: 28034994]
29. Kinoshita Y, Yokota A. Absolute concentrations of metabolites in human brain tumors using in vitro proton magnetic resonance spectroscopy. *Nmr in Biomedicine*. 1997;10(1):2–12. [PubMed: 9251109]
30. Nascimento RAS, Ozel RE, Mak WH, Mulato M, Singaram B, Pourmand N. Single Cell “Glucose Nanosensor” Verifies Elevated Glucose Levels in Individual Cancer Cells. *Nano Letters*. 2016;16(2):1194–1200. [PubMed: 26752097]
31. Pfeuffer J, Tkac I, Gruetter R. Extracellular-intracellular distribution of glucose and lactate in the rat brain assessed noninvasively by diffusion-weighted H-1 nuclear magnetic resonance spectroscopy in vivo. *J Cerebr Blood F Met*. 2000;20(4):736–746.
32. Obara-Michlewska M, Szeliga M. Targeting Glutamine Addiction in Gliomas. *Cancers*. 2020;12(2).
33. Ye ZC, Sontheimer H. Glioma cells release excitotoxic concentrations of glutamate. *Cancer Research*. 1999;59(17):4383–4391. [PubMed: 10485487]
34. Noch E, Khalili K. Molecular mechanisms of necrosis in glioblastoma The role of glutamate excitotoxicity. *Cancer Biol Ther*. 2009;8(19):1791–1797. [PubMed: 19770591]

35. Zamecnik J The extracellular space and matrix of gliomas. *Acta Neuropathologica*. 2005;110(5):435–442. [PubMed: 16175354]
36. Schmidt KC, Turkheimer FE. Kinetic modeling in positron emission tomography. *Quarterly Journal of Nuclear Medicine*. 2002;46(1):70–85.
37. Huang SC, Phelps ME, Hoffman EJ, Sideris K, Selin CJ, Kuhl DE. Noninvasive determination of local cerebral metabolic rate of glucose in man. *Am J Physiol*. 1980;238(1):E69–82. [PubMed: 6965568]
38. Bociek S, Franks F. Proton-Exchange in Aqueous-Solutions of Glucose - Hydration of Carbohydrates. *J Chem Soc Farad T 1*. 1979;75:262–270.
39. Zaiss M, Anemone A, Goerke S, et al. Quantification of hydroxyl exchange of D-Glucose at physiological conditions for optimization of glucoCEST MRI at 3, 7 and 9.4 Tesla. *Nmr in Biomedicine*. 2019;32(9).
40. Ellingson BM, Yao JW, Raymond C, et al. pH-weighted molecular MRI in human traumatic brain injury (TBI) using amine proton chemical exchange saturation transfer echoplanar imaging (CEST EPI). *Neuroimage-Clin*. 2019;22.
41. Khlebnikov V, van der Kemp WJM, Hoogduin H, Klomp DWJ, Prompers JJ. Analysis of chemical exchange saturation transfer contributions from brain metabolites to the Z-spectra at various field strengths and pH. *Sci Rep-Uk*. 2019;9.
42. Haris M, Singh A, Cai KJ, et al. A technique for in vivo mapping of myocardial creatine kinase metabolism. *Nature Medicine*. 2014;20(2):209–214.
43. Cai KJ, Tain RW, Zhou XHJ, et al. Creatine CEST MRI for Differentiating Gliomas with Different Degrees of Aggressiveness. *Molecular Imaging and Biology*. 2017;19(2):225–232. [PubMed: 27541025]
44. Zhou Z, Nguyen C, Chen Y, et al. Optimized CEST cardiovascular magnetic resonance for assessment of metabolic activity in the heart. *J Cardiovasc Magn Reson*. 2017;19(1):95. [PubMed: 29191206]
45. Wyss M, Braissant O, Pischel I, et al. Creatine and creatine kinase in health and disease--a bright future ahead? *Subcell Biochem*. 2007;46:309–334. [PubMed: 18652084]
46. Goerke S, Zaiss M, Bachert P. Characterization of creatine guanidinium proton exchange by water-exchange (WEX) spectroscopy for absolute- pH CEST imaging in vitro. *Nmr in Biomedicine*. 2014;27(5):507–518. [PubMed: 24535718]
47. Goerke S, Zaiss M, Bachert P. Characterization of creatine guanidinium proton exchange by water-exchange (WEX) spectroscopy for absolute-pH CEST imaging in vitro. *NMR Biomed*. 2014;27(5):507–518. [PubMed: 24535718]
48. Zhou JY, Yan K, Zhu H. A Simple Model for Understanding the Origin of the Amide Proton Transfer MRI Signal in Tissue. *Appl Magn Reson*. 2012;42(3):393–402. [PubMed: 23243339]
49. Kanazawa Y, Fushimi Y, Sakashita N, Okada T, Arakawa Y, Miyazaki M. B-1 Power Optimization for Chemical Exchange Saturation Transfer Imaging: A Phantom Study Using Egg White for Amide Proton Transfer Imaging Applications in the Human Brain. *Magn Reson Med Sci*. 2018;17(1):86–94. [PubMed: 28566586]
50. Zhou J, Payen J-F, Wilson DA, Traystman RJ, van Zijl PC. Using the amide proton signals of intracellular proteins and peptides to detect pH effects in MRI. *Nature medicine*. 2003;9(8):1085.
51. Liu DP, Zhou JY, Xue R, Zuo ZT, An J, Wang DJJ. Quantitative Characterization of Nuclear Overhauser Enhancement and Amide Proton Transfer Effects in the Human Brain at 7 Tesla. *Magnetic Resonance in Medicine*. 2013;70(4):1070–1081. [PubMed: 23238951]
52. Xu JD, Yadav NN, Bar-Shir A, et al. Variable Delay Multi-Pulse Train for Fast Chemical Exchange Saturation Transfer and Relayed-Nuclear Overhauser Enhancement MRI. *Magnetic Resonance in Medicine*. 2014;71(5):1798–1812. [PubMed: 23813483]
53. Xu X, Chan KWY, Knutsson L, et al. Dynamic Glucose Enhanced (DGE) MRI for Combined Imaging of Blood-Brain Barrier Break Down and Increased Blood Volume in Brain Cancer. *Magnetic Resonance in Medicine*. 2015;74(6):1556–1563. [PubMed: 26404120]
54. Xu X, Yadav NN, Knutsson L, et al. Dynamic Glucose-Enhanced (DGE) MRI: Translation to Human Scanning and First Results in Glioma Patients. *Tomography*. 2015;1(2):105–114. [PubMed: 26779568]

55. Kwan EE. Factors affecting the relative efficiency of general acid catalysis. *J Chem Educ.* 2005;82(7):1026–1030.
56. Roy B, Depaix A, Perigaud C, Peyrottes S. Recent Trends in Nucleotide Synthesis. *Chem Rev.* 2016;116(14):7854–7897. [PubMed: 27319940]
57. Warweg E, Stearns G. Studies of Phosphorus of Blood. Ii. The Partition of Phosphorus in Blood in Relation to the Corpuscle Volume. *J Clin Invest.* 1934;13(3):411–418. [PubMed: 16694218]
58. Buchli R, Martin E, Boesiger P, Rumpel H. Developmental-Changes of Phosphorus Metabolite Concentrations in the Human Brain - a P-31 Magnetic-Resonance Spectroscopy Study in-Vivo. *Pediatr Res.* 1994;35(4):431–435. [PubMed: 8047379]
59. Sharma S, Hashmi MF, Castro D. Hypophosphatemia. In: *StatPearls.* Treasure Island (FL) 2020.
60. Williams RH, Wilson JD. *Williams textbook of endocrinology.* 9th ed. Philadelphia: Saunders; 1998.
61. Kemp GJ, Meyerspeer M, Moser E. Absolute quantification of phosphorus metabolite concentrations in human muscle in vivo by P-31 MRS: a quantitative review. *Nmr in Biomedicine.* 2007;20(6):555–565. [PubMed: 17628042]
62. Ren J, Sherry AD, Malloy CR. (31)P-MRS of healthy human brain: ATP synthesis, metabolite concentrations, pH, and T1 relaxation times. *NMR Biomed.* 2015;28(11):1455–1462. [PubMed: 26404723]
63. McElroy WD. *Phosphorus metabolism; a symposium on the role of phosphorus in the metabolism of plants and animals.* Baltimore,: Johns Hopkins Press; 1951.
64. Hetherington HP, Spencer DD, Vaughan JT, Pan JW. Quantitative (31)P spectroscopic imaging of human brain at 4 Tesla: assessment of gray and white matter differences of phosphocreatine and ATP. *Magn Reson Med.* 2001;45(1):46–52. [PubMed: 11146485]
65. Dawson RMC. *Data for biochemical research.* Oxford: Clarendon Press; 1959.
66. Auerbach S, Young W. Total phosphate determination in brain tissues: a method for regional determination of total phosphate in rat brain. *Cent Nerv Syst Trauma.* 1987;4(1):53–61. [PubMed: 3301010]

**Figure 1.**

Simulation of dynamic glucose enhancement (DGE) time signal. The compartmental model of DGE were demonstrated in **A**. **B** showed the arterial input function and the extracellular and intracellular compartment concentration time curve simulated with a compartmental DGE kinetics model. The total tissue concentration was calculated as the sum of extracellular and intracellular concentration. Solid lines represented the time curves of normal white matter tissue, and the dashed lines represented time curves of tumor tissue. The kinetics model was then used to simulate DGE signal change over time, as demonstrated in **C**.

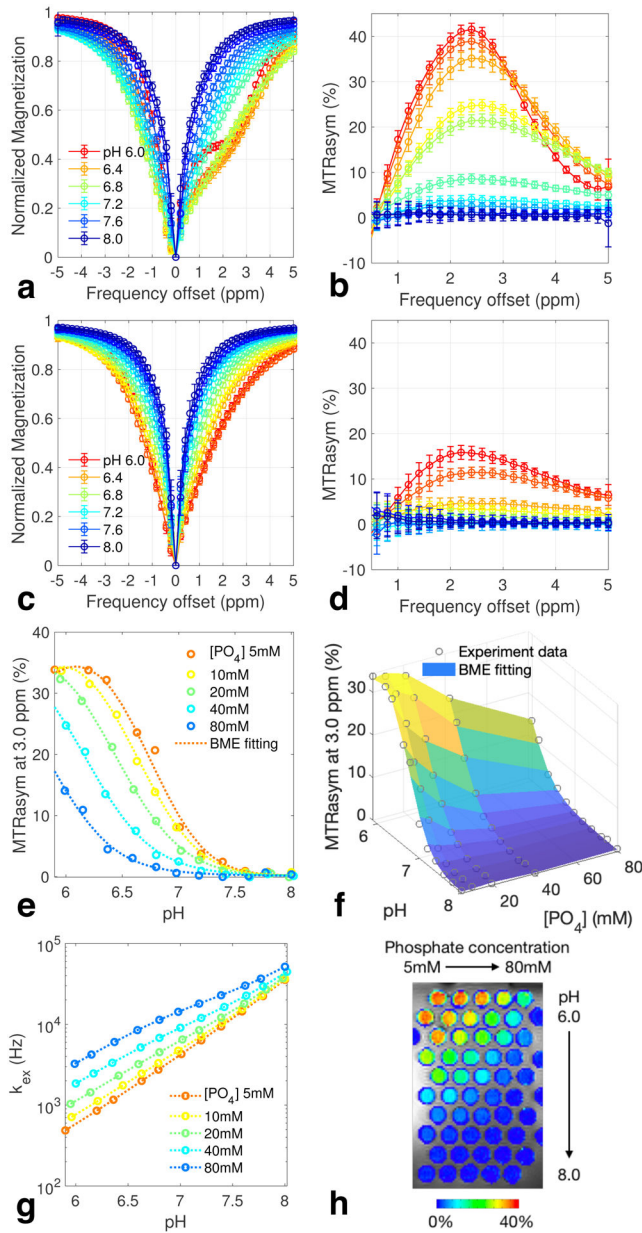


Figure 2.

Glycine phantom experiment data and Bloch-McConnell simulation fitting results. **A** and **B** show the z-spectra and MTR_{asyM} of phantom solutions of different pH with phosphate concentration of 5 mM. **C** and **D** show the z-spectra and MTR_{asyM} experiment data with phosphate concentration of 80 mM. All data points were represented with mean and error bar of standard deviation. The MTR_{asyM} at 3.0 ppm of each phantom sample and the Bloch-McConnell equation fitting results were plotted in **E** and **F**. Using the fitted exchange rate parameters, the proton exchange rates were calculated for each sample and plotted in **G**. **H** showed a colored map of MTR_{asyM} at 3.0 ppm at one slice.

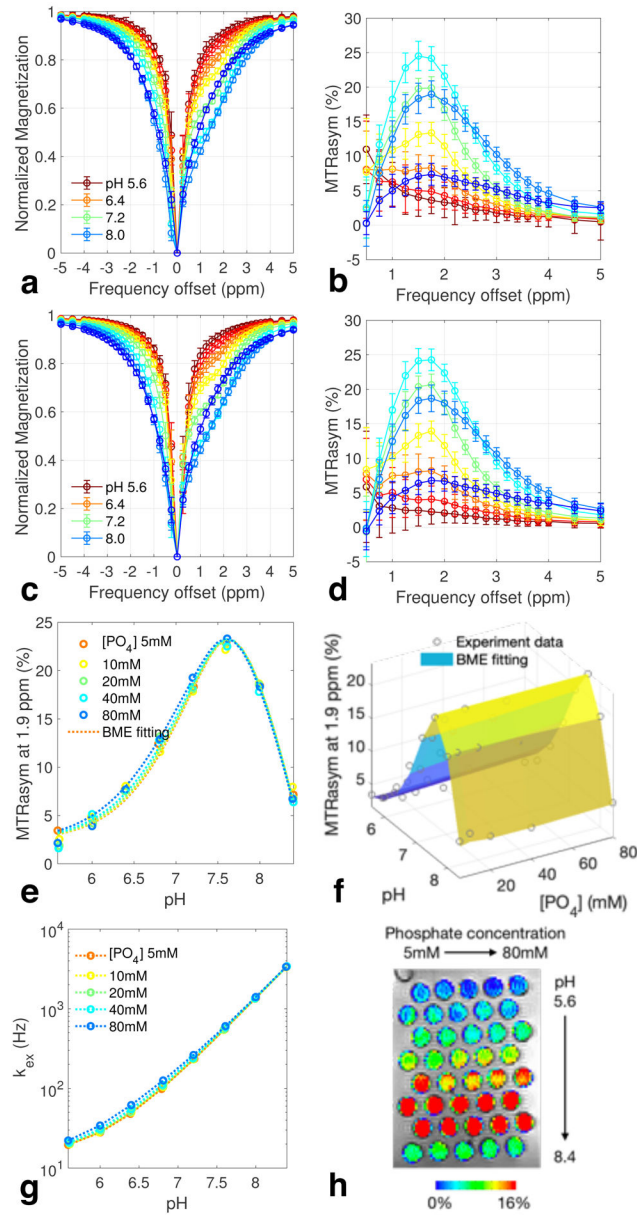


Figure 3. Creatine phantom experiment data and Bloch-McConnell simulation fitting results. **A** and **B** show the z -spectra and MTR_{asym} of phantom solutions of different pH with phosphate concentration of 5 mM. **C** and **D** show the z -spectra and MTR_{asym} experiment data with phosphate concentration of 80 mM. All data points were represented with mean and error bar of standard deviation. The MTR_{asym} at 1.9 ppm of each phantom sample and the Bloch-McConnell equation fitting results were plotted in **E** and **F**. Using the fitted exchange rate parameters, the proton exchange rates were calculated for each sample and plotted in **G**. **H** showed a colored map of MTR_{asym} at 1.9 ppm at one slice.

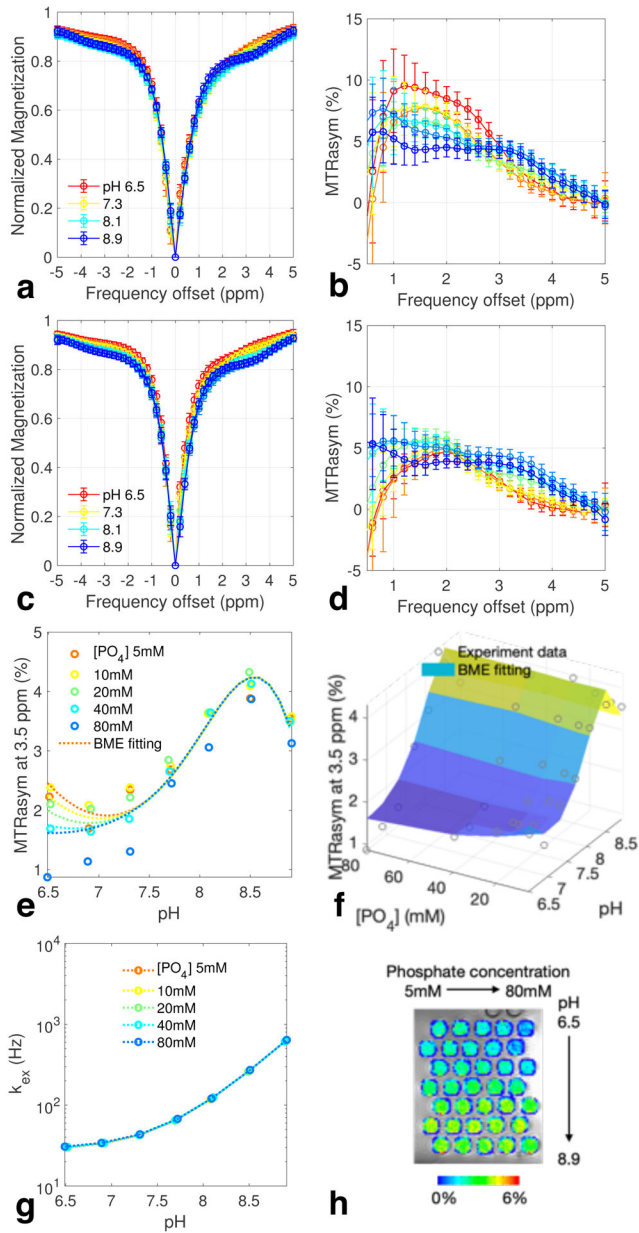


Figure 4. Egg white protein phantom experiment data and Bloch-McConnell simulation fitting results. **A** and **B** show the z -spectra and MTR_{asym} of phantom solutions of different pH with phosphate concentration of 5 mM. **C** and **D** show the z -spectra and MTR_{asym} experiment data with phosphate concentration of 80 mM. All data points were represented with mean and error bar of standard deviation. The MTR_{asym} at 3.5 ppm of each phantom sample and the Bloch-McConnell equation fitting results were plotted in **E** and **F**. Using the fitted exchange rate parameters, the proton exchange rates were calculated for each sample and plotted in **G**. **H** showed a colored map of MTR_{asym} at 3.5 ppm at one slice.

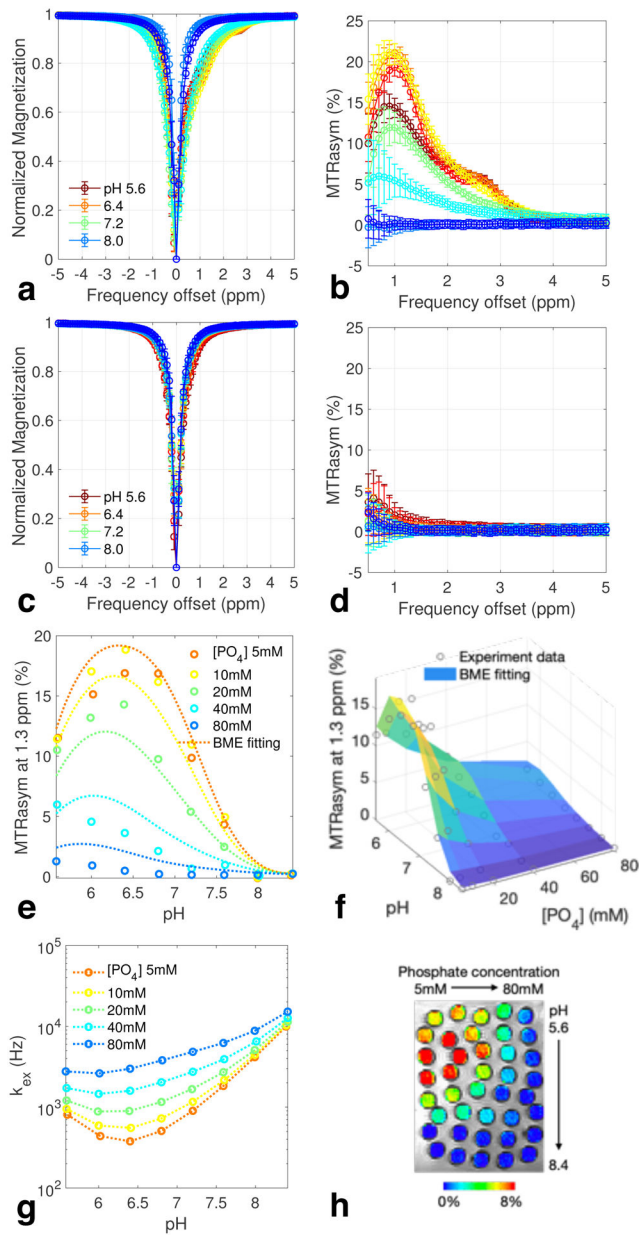


Figure 5.

Glucose phantom experiment data and Bloch-McConnell simulation fitting results. **A** and **B** show the z -spectra and MTR_{asym} of phantom solutions of different pH with phosphate concentration of 5 mM. **C** and **D** show the z -spectra and MTR_{asym} experiment data with phosphate concentration of 80 mM. All data points were represented with mean and error bar of standard deviation. The MTR_{asym} at 1.3 ppm of each phantom sample and the Bloch-McConnell equation fitting results were plotted in **E** and **F**. Using the fitted exchange rate parameters, the proton exchange rates were calculated for each sample and plotted in **G**. **H** showed a colored map of MTR_{asym} at 1.3 ppm at one slice.

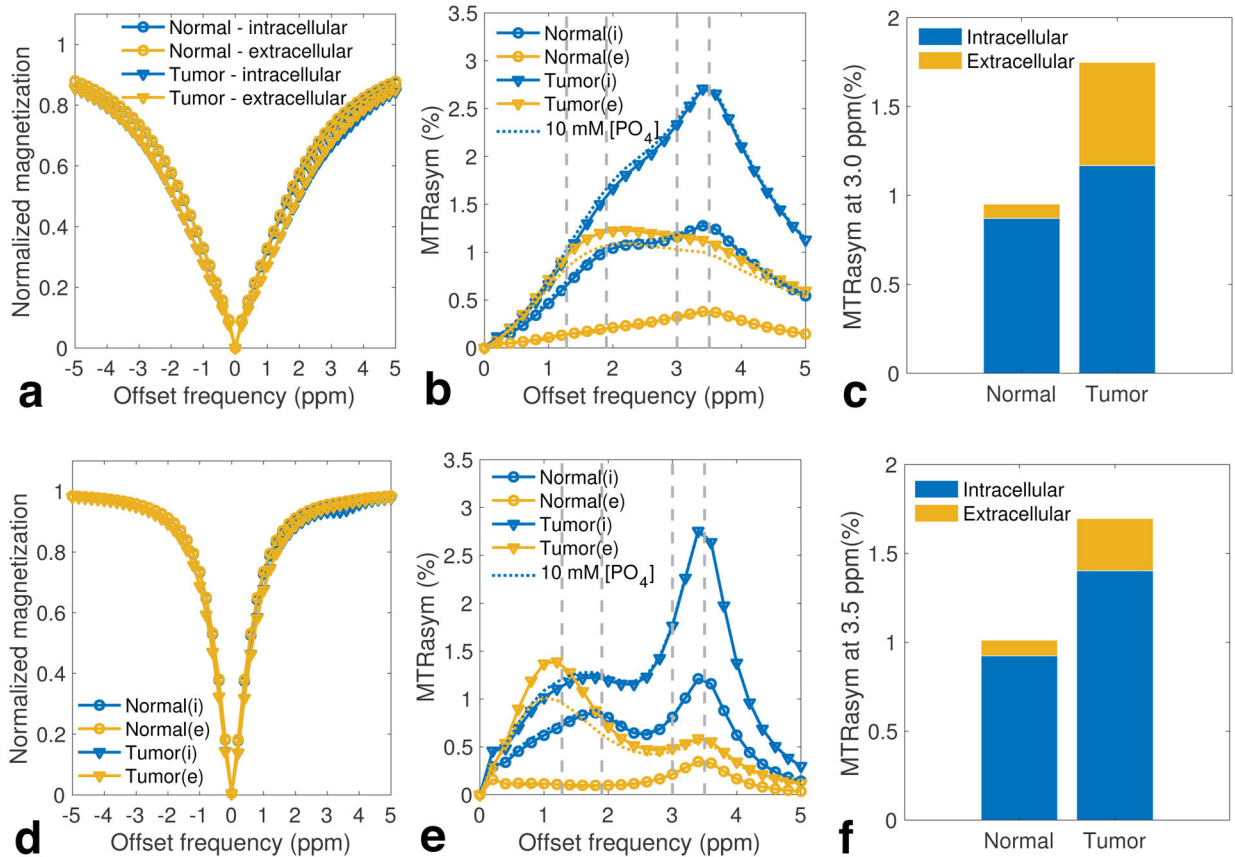


Figure 6.

Simulation of amine and amide CEST signal in the intracellular and extracellular compartment of normal white matter and brain tumor. **A** and **B** showed the z -spectra and MTR_{asym} of the simulated amine CEST effect. The MTR_{asym} at 3.0 ppm contrast contributed from intra- and extracellular compartment was stack plotted in **C**. **D** and **E** illustrated the z -spectra and MTR_{asym} of the simulated amide CEST effect, with the MTR_{asym} at 3.5 ppm contrast contributed from intra- and extracellular compartment stack plotted in **F**. In **B** and **E**, the gray dashed lines represented the offset frequencies of four exchangeable protons pools ($-\text{OH}$: 1.28 ppm, $-\eta\text{NH}_2$: 1.9 ppm, $-\alpha\text{NH}_2$: 3.0 ppm, $-\text{NH}$: 3.5 ppm). Solid blue and yellow lines represented the simulated MTR_{asym} assuming intracellular phosphate concentration of 20 mM and extracellular concentration of 1 mM. Dashed blue and yellow lines represented the simulated MTR_{asym} assuming intracellular and extracellular phosphate concentration of 10 mM.

Table 1.

Sample preparation for phantom experiments

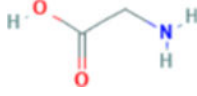
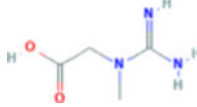
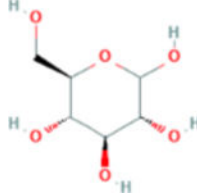
Phantom species	Glycine	Creatine	Egg white protein	Glucose
Molecular structure			Ovalbumin (54%), Ovotransferrin (12%), Ovomuroid (11%), Globulin (8%), etc.	
Exchangeable proton	Amine $-\alpha\text{NH}_2$	Amine $-\eta\text{NH}_2$	Amine $-\alpha\text{NH}_2$ Amide $-\text{NH}$	Hydroxyl $-\text{OH}$
Species concentration	100 mM	50 mM	~10% protein	100mM
Phosphate concentration				5, 10, 20, 40, 80 mM
pH	6.0 to 8.0 with 0.2 interval	5.6 to 8.4 with 0.4 interval	6.5 to 8.9 with 0.4 interval	5.6 to 8.4 with 0.4 interval

Table 2.

Parameters used in computer simulation of CEST signal and dynamic glucose enhanced (DGE) time curve.

Simulation – tissue parameters					
	Normal (intracellular)	Tumor (intracellular)	Normal (intracellular)	Tumor (intracellular)	
$T_{1,\text{water}}$ (s)	0.832	1.558	0.832	1.558	
$T_{2,\text{water}}$ (s)	0.110	0.160	0.110	0.160	
pH	7.0	7.2	7.4	6.6	
Phosphate (mM)	20	20	1	1	
Amine αNH_2 (mM)	20	24	10	20	
Amide NH (mM)	70	84	15	18	
Amine ηNH_2 (mM)	20	16	0.1	0.1	
Hydroxyl OH (mM)	15	30	15	30	
Simulation – sequence parameters					
Saturation pulse	Amine CEST		Amide CEST		DGE
Pulse shape	Gaussian		Gaussian		Gaussian
Peak B_1 amplitude (μT)	4.206		1.402		1.402
Pulse duration (ms)	100		100		100
Pulse number	3×10		3×10		3×10
Simulation – DGE dynamic model parameters					
Exchange parameters	k_1	k_2	k_3	k_4	k_5
Normal white matter	0.0540	0.1090	0.0500	0.0050	0.0450
Tumor tissue	0.1020	0.1300	0.1000	0.0100	0.0620

Table 3.

Phantom parameter estimations using Bloch-McConnell simulation fitting

Phantom species	Glycine	Creatine	Egg white protein	Glucose
Exchangeable proton	Amine α -NH ₂	Amine η -NH ₂	Amine α -NH ₂ , Amide γ -NH	Hydroxyl-OH
Fitted proton concentration (mM) [Confidence interval (CI)]	181.73 [176.46 – 187.00]	134.33 [130.58 – 138.17]	NH ₂ : 46.44 [11.01 – 81.88] NH: 46.46 [34.21 – 36.34] Macromolecule: (fraction) 3.45×10 ⁻⁶ [3.23×10 ⁻⁶ – 3.66×10 ⁻⁶]	267.32 [204.05 – 330.59]
Fitted water pool T ₂ (s) [CI]	1.48 [1.36 – 1.60]	2.37 [2.22 – 2.52]	0.35 [0.34 – 0.35]	1.49 [1.20 – 1.78]
Fitted exchange rate constant k ₀ (s ⁻¹) [CI]	58.31 [0 – 146.66] ^a	14.14 [9.08 – 19.21]	27.41 [15.44 – 39.38]	0 ^b [0 – 172.06] ^a
Fitted exchange rate constant k _a (s ⁻¹ M ⁻¹) [CI]	N/A	N/A	N/A	2.64×10 ⁸ [1.64×10 ⁸ – 3.64×10 ⁸]
Fitted exchange rate constant k _b (s ⁻¹ M ⁻¹) [CI]	3.45×10 ¹⁰ [3.18×10 ¹⁰ – 3.71×10 ¹⁰]	1.34×10 ⁹ [1.28×10 ⁹ – 1.41×10 ⁹]	7.53×10 ⁷ [6.34×10 ⁷ – 8.73×10 ⁷]	3.93×10 ⁹ [2.50×10 ⁹ – 5.36×10 ⁹]
Fitted exchange rate constant k _{cA} (s ⁻¹ M ⁻¹) [CI]	2.26×10 ⁵ [2.02×10 ⁵ – 2.50×10 ⁵]	630.43 [105.79 – 1.16×10 ³]	8.52 [0 – 332.44] ^a	6.46×10 ⁴ [3.46×10 ⁴ – 9.45×10 ⁴]
Fitted exchange rate constant k _{cB} (s ⁻¹ M ⁻¹) [CI]	7.55×10 ³ [2.24×10 ³ – 1.29×10 ⁴]	0 ^b [0 – 154.36] [*]	13.92 [0 – 400.55] ^a	2.35×10 ⁴ [1.25×10 ⁴ – 3.45×10 ⁴]
R ² of fitting	1.00	0.99	0.90	0.95
Exchange rate k _{ex} (pH = 7, [PO ₄] = 10 mM)	k _{ex} = 1.01×10 ⁴ s ⁻¹	k _{ex} = 355.60 s ⁻¹	k _{ex} = 46.44 s ⁻¹	k _{ex} = 1.50×10 ³ s ⁻¹
Change in k _{ex} with 50 mM phosphate at pH 7	k _{ex} = 6.95×10 ³ s ⁻¹	k _{ex} = 18.98 s ⁻¹	k _{ex} = 0.53 s ⁻¹	k _{ex} = 2.41×10 ³ s ⁻¹

^aConfidence interval crosses zero. Due to the non-negative nature of fitting parameters, the lower confidence intervals were truncated to zero.^bExchange rate constant k < 10⁻² sec⁻¹M⁻¹ or k < 10⁻² sec⁻¹

Table 4.List of pK_a values and concentrations of inorganic phosphate and common organic phosphate.

	Number of PO ₄ groups	pK _a	Concentration in brain (intracellular) ^a	Concentration in muscle (intracellular) ^a
<i>Inorganic phosphate</i>				
H ₂ PO ₄ ⁻ /HPO ₄ ²⁻	1	6.82	Extracellular: 1 mM Intracellular: 1–2 mM ⁶⁰	Total: 4.6 mM ⁶¹
<i>Organic phosphate - monophosphates</i>				
PE	1	6.5 ^b	3.03 mM ⁶²	/
PC	1	6.5 ^b	0.40 mM ⁶²	/
GPE	1	1.5 ^c	1.07 mM ⁶²	/
GPC	1	1.5 ^c	1.76 mM ⁶²	/
PCr	1	4.5 ⁶³	5.83 mM ⁶²	33.87 mM ⁶⁴
AMP	1	6.1 ⁶⁵	/	/
<i>Organic phosphate – diphosphates</i>				
NAD	2	6.5 ^d	0.37 mM ⁶²	/
UDPG	2	6.5 ^d	0.11 mM ⁶²	/
ADP	2	6.3 ⁶⁵	/	/
<i>Organic phosphate – triphosphates</i>				
ATP	3	6.5 ⁶⁵	4.12 mM ⁶²	11.33 mM ⁶⁴
<i>Phosphate bound to large molecules</i>				
Phospholipid	1	1.5 ^c	/	/
Phosphorylated protein	1-multiple	6.5 ^b	/	/
DNA, RNA	multiple	1.5 ^c	/	/
<i>Total metabolite phosphate measured by ³¹P-MRS in healthy human brains⁵⁸</i>				
Neonates: 14.9 mM; Infants: 16.1 mM, Adults: 29.3 mM				
<i>Total phosphate (including bounded phosphate) measured in rat brain biopsy⁶⁶</i>				
148.47 mM				

Abbreviations: PE, phosphoethanolamine; PC, phosphocholine, GPE, glycerophosphoethanolamine; GPC, glycerophosphocholine; PCr: phosphocreatine; AMP: adenosine monophosphate; NAD: nicotinamide adenine dinucleotide; UDPG: uridine diphosphate glucose; ADP: adenosine diphosphate; ATP: adenosine triphosphate; DNA: deoxyribonucleic acid; RNA: ribonucleic acid.

^aThe tissue concentrations reported by literature were converted to intracellular concentration using the assumptions that organic phosphate remains intracellular and that intracellular space occupies ¾ of the tissue.

^bThe pK_a of phosphate monoesters was adopted.⁵⁶

^cThe pK_a of phosphate diesters was adopted.⁵⁶

^dThe pK_a of pyrophosphate diesters was adopted.⁵⁶